**Arab American University – Jenin**

**Faculty of Graduate Studies**

# Design and characterization of $WO_3$/Li/$WO_3$ heterojunction devices

By

**Shorooq Sameer Mihdawi**

Supervisor

**Dr. Muayad Abu Saa & Prof. Dr. Hazem Khanfar**

This Thesis was submitted in partial fulfillment of the requirements for

**The Master's degree in**

**Physics**

**January 2022**

# Design and characterization of $WO_3/Li/WO_3$ heterojunction devices

By

**Shorooq Sameer Mihdawi**

This thesis was defended successfully on 26th January 2022 and approved by:

Committee members                                        Signature

1. Supervisor: Dr. Muayad Abu Saa …… Muayyad
2. Co-Supervisor: Prof. Dr. Hazem Khanfar …… H.K
3. External Examiner: Prof. Dr. Mohammed ElSaid …… M. Khalil
4. Internal Examiner: Prof. Dr .Atef Fayez Qasrawi ……

# Declaration

The work provided in this thesis, unless otherwise referenced, is the researcher's own work, and has not been submitted elsewhere for any other degree or qualification.

العمل المقدم في هذه الرسالة، ما لم تتم الاشارة الى غير ذلك، هو عمل الباحث الخاص ولم يتم تقديمه في أي مكان اخر للحصول على أي درجة أو مؤهل اخر.

Student's Name: Shorooq Sameer Mihdwai

Signature: Shorooq Sameer

Data: 10-5-2022

To My Parents

# Acknowledgments

In the name of God, all success is only by Allah.

I would like to thank and appreciate all faculty members. In particular, the honorable Professor Dr. Atef Qasrawi the head of scientific research lab at physics department also I like to give my thanks to my supervisors Dr. Muayad Abu Saa & Prof. Dr. Hazem Khanfar. They made grateful efforts in my thesis and commenting on it with valuable notes to appear in its final form. All thanks and love to my family who supported me all the time. My dear parents, who fight this world to make me a success girl.

Thank are also due to the kind help for both assistances Rana Daraghmeh, and Olfat Omaraya who provided me with support, both in the practical and theoretical sides throughout the work …, all appreciation to all those who provided me the possibility to complete this work.

# Abstract

## Design and characterization of $WO_3$/Li/$WO_3$ heterojunction devices

By

**Shorooq Sameer Mihdawi**

Supervisor

**Dr. Muayad Abu Saa & Prof. Dr. Hazem Khanfar**

In this thesis, we targeted exploring the effects of lithium nano sheet on the structural and electrical properties of $WO_3$ films. The $WO_3$ films which are coated by the thermal evaporation technique under a vacuum pressure of $10^{-5}$ mbar are highly influenced by the Li nano sheet. Namely, Insertion of Li nano sheets of thicknesses of 50 and 100 nm resulted in metal induced crystallization process. Two structural phases evaluated because of Li nano sheet sandwiching. The induced crystallization process is owed to the large lattice mismatch between films and substrates and films and nano sheets. In addition, the electrical investigation which were carried out by the impedance spectroscopy technique have shown that; stacked layers of tungsten oxide comprising Li nano sheets can perform as microwave resonators. Resonance anti-resonance phenomena is observed in the samples. Moreover, the capacitance spectra which we studied in the frequency domain of 0.01-1.8 GHz have shown the dominants of negative capacitance effect. This effect is beneficial for parasitic capacitance cancellation and noise reduction in electronic circuits. Furthermore, the WO3/Li/WO3 device seems to be used in application as thin film MOSFET that can be used digital and analog circuits.

# Contents

| Title | | Page |
|---|---|---|
| List of Tables | | viii |
| List of Figures | | x |
| List of Symbols | | ix |
| Chapter One | Introduction and Literature Survey | 1 |
| Chapter Two | Theoretical Approach | 4 |
| | 2.1 The X-ray Diffraction | 4 |
| | 2.2 Bragg's Law | 4 |
| | 2.3 Scherrer Equations: | 5 |
| | 2.4 Structural Proprieties | 6 |
| | 2.5 Impedance Spectroscopy | 9 |
| | 2.5.1 Series RLC Circuit | 9 |
| | 2.5.2 Capacitance and conductance analysis | 12 |
| | 2.5.3 Frequency Dependent Conductivity | 15 |
| Chapter Three | Experiment Details | 17 |
| | 3.1 Thin Film evaporation | 17 |
| | 3.2 XRD System | 19 |
| | 3.3 Spectroscopy Experiment Details | 19 |
| | 3.4 Current-Voltage Measurements | 20 |
| | 3.5 Hot Probe Technique | 21 |
| Chapter Four | Result and Discussion | 22 |

4.1 Structural X-ray Diffraction (XRD) Characterization 22
4.2 Impedance Spectroscopy 25
4.2.1 Capacitance Spectroscopy 25
4.2.2 Conductance Spectroscopy 29
4.3 Current-Voltage Characteristics 31
Chapter Five Conclusion 33
References 34
الملخص 38

## List of Tables

| No | Title | Page |
|---|---|---|
| (2.1) | The 3-D Bravais lattices for solid-state materials and their conditions | 7 |
| (2.2) | The 14 lattice types shape of Bravais lattice in three dimensions | 8 |
| (4.1) | Scherrer equation for Nano scale crystallites of the sample $WO_3LiWO_3$-100nm | 24 |
| (4.2) | Modeled capacitance variables for AuWWC,AuWLWC-50-, AUWLWC-100-. | 27 |
| (4.3) | Modeled conductivity variables for AuWWC | 31 |

## List of Figures

| No | Caption | Page No |
|---|---|---|
| (2.1) | The schematic diagram of Bragg's law | 5 |
| (2.2) | Series RLC circuit | 9 |
| (2.3) | Current-Voltage relation of series RLC circuit | 10 |
| (2.4) | The impedance triangle of a series RLC circuit | 11 |
| (3.1) | 3D sketch of the thin films of $WO_3$and$WO_3$Li$WO_3$ | 17 |
| (3.2) | The 600 VCM evaporation system | 18 |
| (3.3) | The Rigaku MiniFlex 600 X-ray unit. | 19 |
| (3.4) | Agilent 4291B RF impedance analyzer | 20 |
| (3.5) | The current (I)-voltage (V) characteristic analysis. | 21 |
| (4.1) | XRD patterns of $WO_3$: Li thin films for different Li thickness | 22 |
| (4.2) | The Capacitance spectra of (a) AuWWC, (b) AuWLWC-50-, and (c) AuWLWC-100- samples | 26 |
| (4.3) | The modelled curve of the capacitance of (a) AuWWC, (b) AuWLWC-50-, and (c) AuWLWC-100- | 28 |
| (4.4) | Conductance spectra of $WO_3$: Li thin films for different Li thickness In the range of 0.01-1.8 GHz | 29 |
| (4.5) | Modeled curve of conductivity of AuWWC sample | 30 |
| (4.6) | The current -voltage characteristics (a) AuWLW-50- (b) AuWLWC-100, and (c) AuWWC | 32 |

## List of Symbols

| Symbol | Symbol Meaning |
|---|---|
| Li | Lithium |
| $WO_3$ | Tungsten Oxide |
| $\lambda$ | Wavelength |
| D | Inter-planner distance |
| $\Theta$ | Bragg angle |
| N | Integer |
| Hkl | Miller indices |
| D | Crystallite size |
| $\beta$ | Full width of the peak at half maximum (FWHM) measured in radians |
| $\varepsilon$ | Lattice strain |
| $\delta$ | Dislocation density |
| SF % | Stacking faults |
| QMT | Quantum mechanical tunneling |
| CBH | Correlated barrier hoping |
| MESFETS | Metal Semiconductor Field Effect Transistors |
| MOSFETs | Metal Oxide Semiconductor Field Effect Transistors |
| NBs | Nanotube bundles |
| DFT | Density-Functional Theory |
| QS | A stabilization of quasi-static |
| FE | Ferroelectric |
| DE | Dielectric |
| SS | sub-threshold slope |
| NC | Negative capacitance |

# Chapter One

## Introduction and Literature Survey

$WO_3$ is an important compound due to its huge application in many fields, such as telecommunications, chemical catalyst, optical devices and electrical communications. For example: It was found that the Pd-$WO_3$ and/or Au-Pd-$WO_3$ nano composites decorated with Au 2.4 wt% and Pd 0.48 wt% showed exemplary sensitivity as sensor [1],whereas the complementarity of the $WO_3$–$TiO_2$ layers, result in complement between each other, thus leading to efficient electro chromic performance [2]. More and more the transfer of mass phenomenon, electrostatic attraction, and reduction reaction were the primary processes for Cr(VI) ions elimination. These findings revealed that the synthesized $WO_3$ exhibited a high potential for wastewater treatment [3]. Also, Modification of $WO_3$ for enhancing toxic gas sensor performances. In addition, the discussion of the sensing mechanism, future opportunities as well as challenges will be addressed thereby can inspire research progress on $WO_3$-based toxic gas detection sensors [4]. In addition $WO_3$ one of the most promising photo catalysts for solar water treatment technology and has a specific attention was paid to its properties [5]. The more preferable of $WO_3$ nanorods with high aspect ratio would be used in advanced ethanol sensor application [6].

There are many techniques to synthesize $WO_3$ films such as $WO_3$ thick films on a rough and smooth glass substrate by hydrothermal method and then heated to a temperature of 400-degree Celcius [7], also nanostructured $WO_3$ thin films were prepared by electron beam evaporation on glass substrate and investigated their ethanol gas sensing properties [8].

Furthermore using $WO_3$ thin films formed by differential scanning calorimetry in the temperature [9]. A facile one-step pulsed-voltage electro deposition PVE is used to prepare nano porous amorphous-crystalline dual-phase tungsten trioxide $WO_3$ thin film [10].

$WO_3$ has much desired proprieties which make it preferable for researchers including the structural and electrical ones. $WO_3$ films appear deep-blue and colorless under the applications of negative and positive electrical fields, respectively. In Li+ electrolyte, the electro chromic features of $WO_3$ films are related to the insertion/extraction behavior of Li+ ions [11]. $WO_3$ varies on its shape according at what acidic and temperature it is composed may be it would be a: monoclinic, tetragonal, cubic, orthorhombic, and hexagonal [12].

Doping $WO_3$ is a target to get good benefits in forming thin films with perfect properties, such as efficient photo catalysts is the main bottleneck in practical applications of photo catalytic degradation of organic pollutants. Herein, N-$WO_3$/$Ce_2S_3$ nanotube bundles (NBs) are synthesized and successfully immobilized on a carbon textile, resulting in a flexible and conducting photo catalyst. Due to the large interfacial area between N-$WO_3$ and $Ce_2S_3$ [13]. Hence, in order to improve the efficiency of photo catalysis, it is necessary to accelerate the transfer of photo-generated electron holes and inhibit their recombination. Based on energy band engineering theory, the band gap of CN is changed by adjusting the doping proportion of B element to better match the energy band of $WO_3$, and the optimal energy band state is achieved [14].

In this thesis, the preparation and the formation of $WO_3$/Li/$WO_3$ heterojunctions will be discussed. Namely, the structural properties will be studied by means of X-ray Rigaku diffractometer. In addition, the impedance measurements, electrical characteristics, and the energy band gap formation will be investigated. In the second chapter, the important theoretical investigations that are needed to determine the physical constants are reported and some of the important derivations are shown. In the third chapter, the experimental details that were carried out during preparation and characterization are reported. In the fourth chapter, we report the important 3 measurements and the related interpretations of the results. In the last chapter, the conclusion remarks are mentioned.

# Chapter Two

# Theoretical Approach

## 2.1 The X-ray Diffraction:

X-ray diffraction analysis helps in determining the nature of the materials whether it is amorphous or crystal, and to estimate some variables such as crystal grain size, broadening, lattice constants, inter planner distance using Bragg law.

## 2.2 Bragg Law:

The hypothesis is to imagine Bragg's diffraction as a reflection of X-rays on the surface of imaginary "mirrors" formed by atomic planes in the crystal lattice (shown as horizontal lines containing scattering centers) in figure (2.1). Due to the repetitive nature of the crystal, these planes would be separated by a constant distance ***d***. The two X-ray beams of wavelength $\lambda$ arrive in phase onto the respective imaginary planes, with an angle of incidence $\boldsymbol{\theta}$, and form a wave front where Bragg law then is

$$2\, d\, sin\theta \;=\; n.\lambda \qquad (2.1)$$

With n = 1, 2, 3……

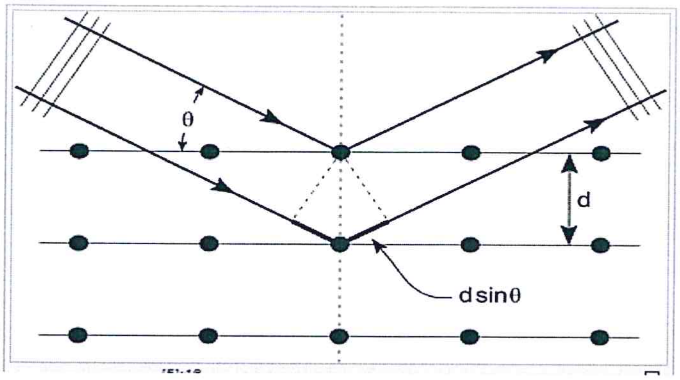

Figure (2.1) The schematic diagram of Bragg's law.

### 2.3 Scherrer Equations:

Scherrer equation is by taking the derivative of Bragg's law, the wavelength constant been vary then Bragg spacing and the diffraction angle to vary, take derivative of Equation (2.1) in $d$ and $\theta$ yields:

$2\Delta d \cos\theta \, \Delta\theta = \lambda$, since $\Delta\theta$ can be positive or negative the absolute value must be taken and it reflects the half-width of the peak so $2\Delta\theta$ is the peak of full-width at half-maximum ($\beta$).

$\Delta d$ reflects the crystallite thickness:

$$\Delta d = \frac{\lambda \beta}{\cos\theta} \qquad (2.2)$$

If a Gaussian function (rather than a triangle function) is used to describe the peak a pre factor of 0.94 occurs so the Scherrer equation is given by

$$t = \frac{0.94\lambda}{\beta \cos\theta} \qquad (2.3)$$

Where $\beta$ is the full-width at half maximum. So,

$$D = \frac{0.94\lambda}{\beta\cos\theta} \tag{2.4}$$

## 2.4 Structural Properties

The X-Ray diffraction pattern shows maximum intensity when the incident wave-vector coincides with the reciprocal lattice vector of the crystal. Thus, a change in intensity correlates to a change in crystallinity [15]. Crystal characteristics such as grain size (D), strain ($\varepsilon$), dislocation density ($\delta$) and stacking faults (SF). These parameters are calculated from the broadening width β (FWHM) of the most intensive peak by using the following relations, Grain size (D) is the diameter of individual grain in the crystal.

$$D = \frac{0.94\lambda}{\beta\cos\theta} \tag{2.5}$$

Strain ($\varepsilon$): is the ratio of contraction or expansion in bonds lengths to the original bonds' lengths

$$\varepsilon = \beta/4\tan\theta \tag{2.6}$$

Dislocation density ($\delta$): is a measure of the total length of dislocation lines per unit area.

$$\delta = 15\varepsilon/aD \text{ (Lines/cm2)} \tag{2.7}$$

Where $a$ is the lattice constant along the a-axis. (SF): is a type of defects which staking faults characterizes the disordering of crystallographic planes. It is considered as planar defect.

$$SF = \frac{2\pi\ 2\beta}{45\sqrt{3}\tan\theta} \tag{2.8}$$

There are fourteen Bravais lattice in 3-dimentional that distributed in seven groups (structures) represented in Table 2.1.

Table (2.1): The 3-D Bravais lattices for solid-state materials and their conditions.

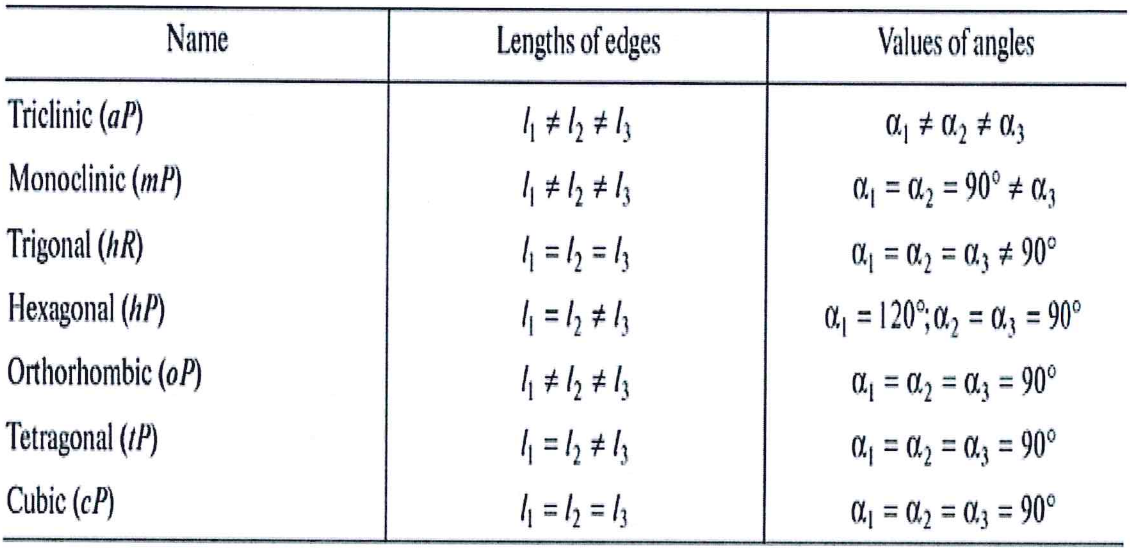

| Name | Lengths of edges | Values of angles |
|---|---|---|
| Triclinic (*aP*) | $l_1 \neq l_2 \neq l_3$ | $\alpha_1 \neq \alpha_2 \neq \alpha_3$ |
| Monoclinic (*mP*) | $l_1 \neq l_2 \neq l_3$ | $\alpha_1 = \alpha_2 = 90^\circ \neq \alpha_3$ |
| Trigonal (*hR*) | $l_1 = l_2 = l_3$ | $\alpha_1 = \alpha_2 = \alpha_3 \neq 90^\circ$ |
| Hexagonal (*hP*) | $l_1 = l_2 \neq l_3$ | $\alpha_1 = 120^\circ; \alpha_2 = \alpha_3 = 90^\circ$ |
| Orthorhombic (*oP*) | $l_1 \neq l_2 \neq l_3$ | $\alpha_1 = \alpha_2 = \alpha_3 = 90^\circ$ |
| Tetragonal (*tP*) | $l_1 = l_2 \neq l_3$ | $\alpha_1 = \alpha_2 = \alpha_3 = 90^\circ$ |
| Cubic (*cP*) | $l_1 = l_2 = l_3$ | $\alpha_1 = \alpha_2 = \alpha_3 = 90^\circ$ |

Table 2.2 The 14 lattice types shape of Bravais lattice in three dimensions.

| **System** | **Bravais Lattice** | | | |
|---|---|---|---|---|
| **Cubic** | 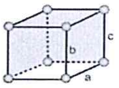 <br>Simple Cubic | 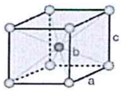 <br>Body centered cubic | 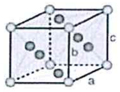 <br>Face centered cubic | |
| **Orthorhombic** | 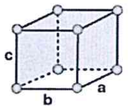 <br>Simple Cubic | 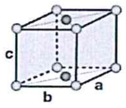 <br>Base centered cubic | 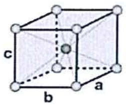 <br>Body centered cubic | 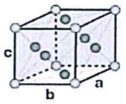 <br>Face centered cubic |
| **Tetragonal** | 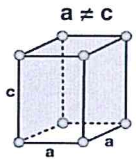 <br>Simple | 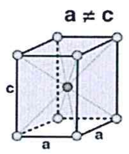 <br>Body centered | | |
| **Monoclinic** | 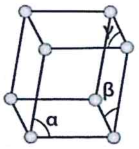 <br>Centered | 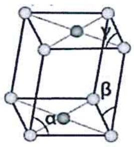 <br>Simple | | |
| **Triclinic** | 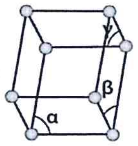 <br>Simple | | | |
| **Trigonal** | 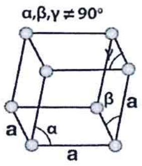 <br>Simple | | | |
| **Hexagonal** | 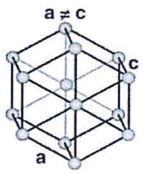 <br>Simple | | | |

## 2.5 Impedance Spectroscopy:

### 2.5.1 Series RLC Circuit

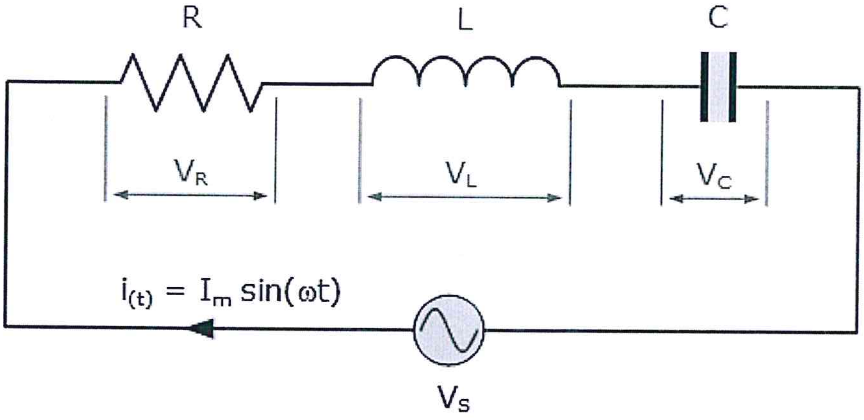

Figure (2.2) Series RLC circuit.

Series RLC circuits consist of a resistance, a capacitance and an inductance connected in series across an alternating supply as shown in figure (2.2). The amplitude of the source voltage across all three components in a series RLC circuit is made up of the three individual component voltages, $V_R$, $V_L$ and $V_C$ with the current common to all three components.

$$V_R = IR \tag{2.9}$$

$$V_L = I\omega L \tag{2.10}$$

$$V_C = \frac{I}{\omega C} \tag{2.11}$$

Where, $I$ is the current, $R$ is the resistance, $\omega$ is the angular frequency of the source, $L$ is the inductance and $C$ is the capacitance. The term $\omega L$ called the inductive reactance and it is denoted by $X_L$. Also, the term of $\frac{1}{\omega C}$ is called the capacitive reactance and denoted by $X_C$.

Since the inductive and capacitive reactance's (XL and XC respectively) are a function of the supply frequency, the sinusoidal response of a series RLC circuit will therefore vary with frequency, *f*. Then the individual voltage drops across each circuit element of R, L and C element will be "out-of-phase" with each other as defined by:

$$I(t) = I_{max}\sin(wt) \tag{2.12}$$

The instantaneous voltage across a pure resistor, $V_R$ is "in-phase" with current. While the instantaneous voltage across a pure inductor, $V_L$ "leads" the current by 90°. The instantaneous voltage across a pure capacitor, $V_C$ "lags" the current by 90°. Therefore, $V_L$ and $V_C$ are 180° "out-of-phase" and in opposition to each other.

For the series circuit in figure (2.2), this is shown in figure (2.4) as:

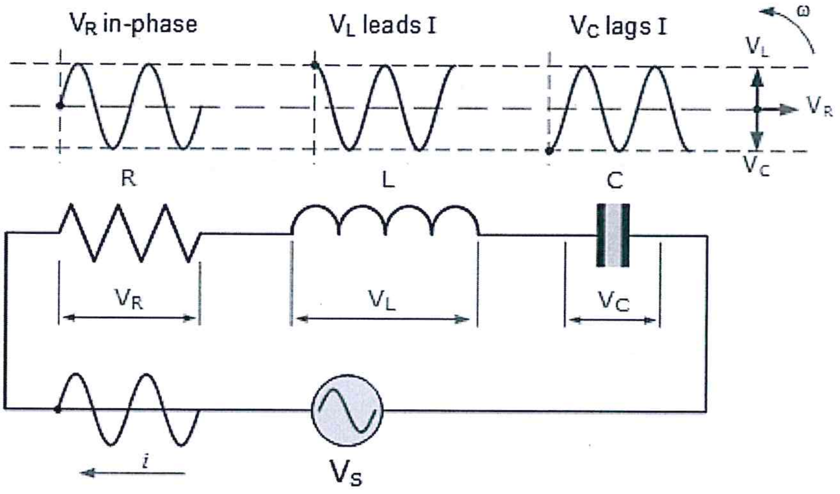

Figure (2.3) Series RLC circuit.

By applying, Kirchhoff's voltage law for both loop and nodal circuits, which states that around any closed loop the sum of voltage drops around the loop equals the sum of the EMF's. This gives us the amplitude of the source voltage, $V_S$ as:

$$V_s = IR + I\omega L + \frac{I}{\omega C} \tag{2.13}$$

The voltage triangle for a series RLC circuit gives that:

$$V_S = ({V_R}^2 + ((V_L - V_C)^2)^{1/2} \tag{2.14}$$

By substituting the values of $V_R$, $V_L$, and $V_C$ into the above equation, $V_S$ will take the form,

$$V_S = I(R^2 + (X_L - X_C)^2)^{1/2} = I \times Z \tag{2.15}$$

Where:

$$Z = (R^2 + (X_L - X_C)^2)^{1/2} \tag{2.16}$$

The amplitude of the source voltage is proportional to the amplitude of the current with proportionality constant called the impedance of the circuit. The overall impedance depends on the resistance and the inductive and capacitive reactance of the circuit by the relation (2.39), which can be represented by an impedance triangle as shown in figure (2.4).

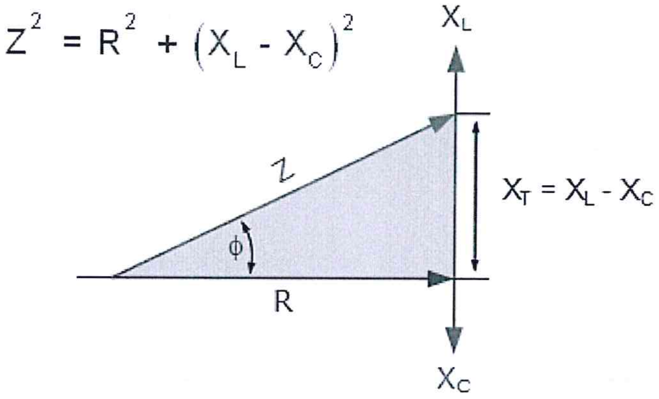

Figure (2.4) The impedance triangle of a series RLC circuit.

The phase angle θ between the source voltage $V_S$ and the current $I$ is the same as for the angle between Z and R in the impedance triangle. The phase angle may be positive or negative in value depending on whether the source voltage leads or lags the circuit current and is calculated from the ohmic values of the impedance triangle as:

$$\cos(\emptyset) = \frac{R}{Z}, \quad \sin(\emptyset) = \frac{(X_L - X_C)}{Z}, \quad \tan(\emptyset) = \frac{(X_L - X_C)}{R} \qquad (2.17)$$

### 2.5.2 Capacitance and Conductance Analysis

Capacitance or admittance spectroscopy gives an insight into the device physics, provided that the experimental data are correctly interpreted, quite often the capacitance exhibits highly non-trivial characteristics, most notable of which is the phenomenon of negative capacitance (NC) [16].

There are three general ways to deal with NC: Firstly, with the incremental charge approach, describing device operation is solved for voltages V and V +ΔV (ΔV is small). The incremental charge distribution in the device δQ(x) is separated into positive and negative components ΔQ and −ΔQ then the capacitance C=ΔQ/ΔV, but there is no rigorous procedure for the separation of incremental charge distribution into positive and negative parts.

Secondly, by the sinusoidal steady-state analysis (SSSA) approach, the system of the time-dependent equations is linearized, but this way needs solution of a system of equations for each frequency to obtain the frequency dependence of capacitance. The third way is the method based on the Fourier analysis involves calculation of the transient response of the device to a small time-dependent voltage excitation (usually in the form of a step-function).

Let consider transient current in a semiconductor device in response to an applied voltage step

$$\delta V \; \delta V(t) \equiv V(t) - V(0-) = \Delta V \, \theta(t) \qquad (2.18)$$

$$\delta I(t) \equiv I(t) - I(0-) = [I(t) - I(\infty)]\,\theta(t) + [I(\infty) - I(0-)]\,\theta(t) \qquad (2.19)$$

Where θ(t) is unit step function, applying that

$$C(\omega) = \frac{1}{\omega} Im\,[Y(\omega)] \qquad (2.20)$$

where $Y(\omega) = \delta I(\omega)/\delta V(\omega)$ is the device admittance relating the small-signal harmonic current flowing through the terminals and small-signal voltage ($\delta I, \delta V \sim e^{i\omega t}$)

The quantities with "+" and "–" superscripts denote single-sided values of the discontinuous functions, for example, $V(0-) = \lim_{\tau \to 0} V(\tau), \tau < 0$.

In equation (2.18) the transient current δI(t) into the step-like component (DC conductivity) and transient current $\delta J(t) = [I(t) - I(\infty)]\,\theta(t)$, so that $\delta J(t) \to 0$ as $t \to \infty$.

Substituting the Fourier expansions of equations (18) & (19) into formula (20), and noting that $\int_{-\infty}^{\infty} \theta(t) e^{-i\omega t}\,dt = 1/(i\omega)$

(Strictly speaking, to ensure convergence of this integral, replace ω by ω − i0), we obtain the following expression for admittance:

$$Y(\omega) = i\omega \int_0^{\infty} \delta I(t)\, e^{-i\omega t}\, dt \qquad (2.21)$$

Separating the real and imaginary parts in formula (2.21), we obtain the expressions for the capacitance and conductance G (ω):

$$C(\omega) = 1/\Delta V \int_0^{\infty} \delta J(t) \cos \omega t\, dt \qquad (2.22)$$

$$G(\omega) = (I(\infty) - I(0-))/\Delta V + \omega/\Delta V \int_0^{\infty} \delta J(t) \sin \omega t\, dt \qquad (2.23)$$

where,

$G(\omega) = \mathrm{Re}\,[Y(\omega)]$.

In general, the transient current $\delta J(t)$ contains an impulse-like component and a slowly varying relaxation component:

$$\delta J(t) = C0\Delta V\,\delta(t) + \delta j(t) \tag{2.24}$$

Here $\delta(t)$ is the delta-function,C0 (which is also called a feed through capacitance or "cold" capacitance), assuming that application of a voltage step results in an instantaneous change of charges on the contacts.

Substituting (2.24) into (2.23) & (2.22) we get:

$$C(\omega) = C0 + (1/\Delta V)\int_0^{\infty} \delta j(t)\cos\omega t\,dt$$

(2.25)

$$G(\omega) = G(0) + (\omega/\Delta V)\int_0^{\infty} \delta j(t)\sin\omega t\,dt \tag{2.26}$$

Using integration by parts, we get:

$$C(\omega) = C0 + (1/\omega\Delta V)\int_0^{\infty}[-(d\delta j(t)/dt])\sin\omega t\,dt$$

(2.27)

$$G(\omega) = G(\infty) + (1/\Delta V)\int_0^{\infty} d\delta j(t)\,dt\,\cos\omega t\,dt$$

(2.28)

Following Atef Qasrawi approach [16] which is based on the charge monotonic/non monotonic variations we assume the presence of two different frequency domains $(w, w_n]$ and $(w- w_p]$

here $w_n$ and $w_p$ are the limits of frequency domains in the n and p- regions, respectively. As a result, equation (2.18) as follows

$$C1 = \Delta Q/\Delta V = (1/\omega\Delta V) \int_0^{\infty}[-(d\delta j(t)/dt])\sin(\omega - wn)t\,dt \tag{2.29}$$

By assuming that the transient response is composed of negative and positive exponential components (arising from charge transport from both sides of the device) given by

$$\delta j(t) = \Delta V(an\,e^{\left(-\frac{t}{tn}\right)} - a_p\,e^{(-t/tp)}) \tag{2.30}$$

and executing the integral of equation (2.29), the C(w) takes the form

$$C(w) = Co + \frac{a1t_n}{(1+(w-wn)^2t_n^2)} - \frac{a1t_p}{(1+(w-wp)^2t_p^2)} \tag{2.31}$$

### 2.5.3 Frequency Dependent Conductivity

In general, the electrical conductivity is proportional to the signal frequency. It is invariably has the form [17], [18],

$$\sigma(\omega) = A\omega^s \tag{2.32}$$

The loss mechanisims should have a wide range of relaxation times $\tau$ in order to give this behaviour of AC conduction. The value of the exponent $s = 1$ indicates that the distribution of relaxation times $n(\tau)$ is inversely proportional to $\tau$ and $\sigma(\omega)$ becomes linearly dependent on frequency. In this case, the relaxation time takes the following form,

$$\tau = \tau_o e^{\xi} \tag{2.33}$$

Where, $\xi$ is a random variable.

The behavior of the conductivity $\sigma_T(\omega)$ usually results from two current conduction mechanisims, the Quantum mechanical tunneling $\sigma_{Tunneling}(\omega)$ and the corellated barrier hoping $\sigma_{CBH}(\omega)$. Thus, the conductivity may take the form,

$$\sigma_T(\omega) = \left(\sigma_{Tunneling}^{-1} + \sigma_{CBH}^{-1}\right)^{-1} \tag{2.34}$$

The Quantum mechanical tunneling (QMT) theory suggests that $\xi = 2\alpha R$. While, in situations where the corollated barrier hoping (CBH) dominates, the random variable is $\xi = \exp\left(-\frac{E_H}{kT}\right)$. Where, $\alpha^{-1}$ is the spatial decay parameter which describes the localized state at each site. $\alpha$ is assumed to be constant for all sites ($\alpha^{-1} \approx 10A^o$), $R$ is the intersite separaetion and $E_H$ is the hopping barrier hight.

$\sigma_{Tunneling}(\omega)$ and $\sigma_{CBH}(\omega)$ are expreesed by the following equations,

$$\sigma_{Tunneling}(\omega) = \frac{\pi^2}{24} kT\alpha^{-1}(N(E_F))^2 \omega R_\omega^2 \tag{2.35}$$

$$\sigma_{CBH}(\omega) = \sigma(H) + \frac{\sigma(L) - \sigma(H)}{1 + (\omega\tau_n)^2} \tag{2.36}$$

In the previous equations, $N(E_F)$ is the density of localized states at the Fermi level, $R_\omega = \frac{1}{2\alpha}\ln(\frac{1}{\omega\tau_o})$ is the hopping distance at a particuler frequency $(\omega)$, $\tau_o$ which is equal to the inverse of the phonon frequency $(v)$, is the charecteristic relaxation time, $\sigma(L)$, $\sigma(H)$ relate to the low- and high- frequency conductivity values, respectively, and $\tau_n = \tau_o \exp\left(-\frac{E_H}{kT}\right)$, where, $E_H$ , as we mentioned befor, is the hight of potential barriers that the hols hope over. The frequency dependence of $\sigma(\omega)$ in equation (2.34) can be deduced by executing the derivative $s = dln(\sigma(\omega))/dln(\omega)$. This gives, for quantam mechanical tunneling ,

$$s = 1 - \frac{4}{\left(\frac{1}{\ln(\omega\tau_o)}\right)} \tag{2.37}$$

The charge carriers transfer by the QMT process when $\sigma(\omega)$ exhibits an increasing trend with frequency and $s$ decreases with increasing frequency [17], [18].

# Chapter Three

# Experiment Details

## 3.1 Thin Film Evaporation

In this work two cycles of evaporating Au/WO3/Li/WO3 /Au with different lithium nano sheet thickness of 50-nm-,100-nm- using VCM-600 evaporation in figure (3.1) technique under vacuum pressure 2x$10^{-4}$ mbar. The steps of evaporation process as follows:

1) A glass slide is cleaned by alcohol then inserted in ultrasonic shaker for about 20 minutes.

2) After that, they dried from alcohol, so the slides were ready to be used in the evaporating system.

3) 0.2gm of $WO_3$ was weighed and inserted in a boat.

4) The slides were attached to the evaporation holder of the evaporation system

Two samples are prepared as follows:

1) Au/$WO_3$-0.5µm-/Li-50nm-/$WO_3$-0.5µm- / Au named as (AuWLWAu-50-)

2) Au/$WO_3$-0.5μm-/Li-100nm-/$WO_3$ -0.5μm-/ Au named as (AuWLWAu-100nm-) was evaporated, through this trial a sample of Au/$WO_3$-0.5μm-/ $WO_3$-0.5μm-/Au named as (AuWWAu) was evaporated without Lithium as illustrated in figure (3.1).

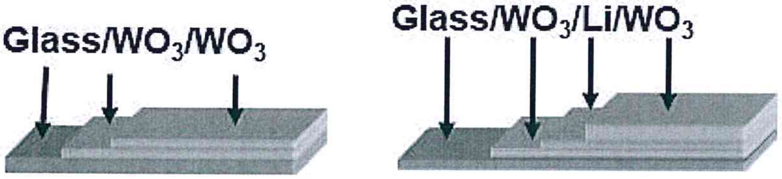

Figure (3.1) 3D sketch of thin films of $WO_3$and $WO_3LiWO_3$.

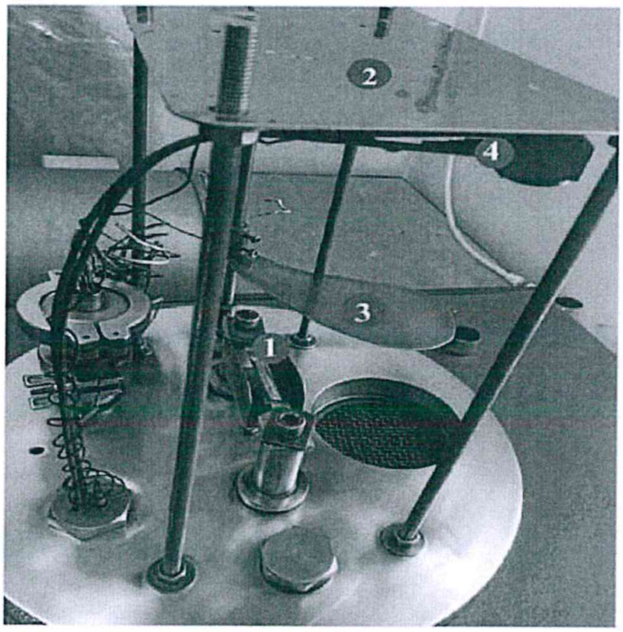

Figure (3.2) The 600 VCM evaporation system.

Thermal evaporation technique is used to form a heterojunction structure. To deposit a tungsten oxide by using evaporation technique as shown in figure (3.1) on a cleaned glass at (item 1). After that, the samples are fixed on a metal plate (item 2) which is located over the evaporation source (item 1). The movable shutter (item 3) which is located between sample and the boat is used to control the evaporation proses through deposition. Quartz crystal monitor (item 4) is used to measure the thickness of tungsten oxide. The second run is a layer of lithium in different thicknesses (0,50 and 100 nm) deposited on a $WO_3$ layer. The final run is a 500 nm $WO_3$ is deposited over the WO3 layer. Thus, ($WO_3$ /Li /$WO_3$) heterojunction is formed.

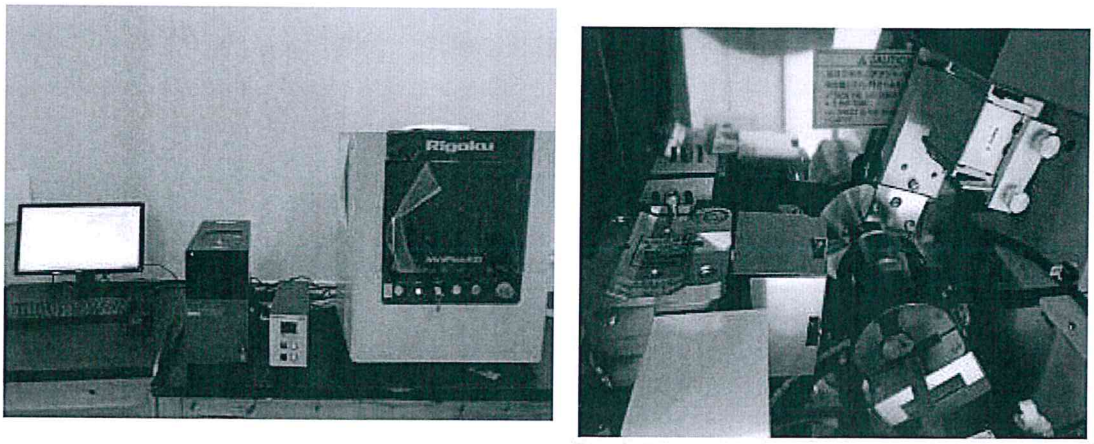

Figure (3.3) The Rigaku MiniFlex 600 X-ray unit.

## 3.2 XRD System

The Rigaku diffractometer shown in figure (3.3) equipped with Kα radiation of a copper anode of average wavelength 1.5405 Å at 40 KV and 15 mA is used to study the crystal nature of $Au/WO_3$-1μm- and $WO_3/Li/WO_3$ interfaces. The 2θ range of 10°-70° with a step 0.1° scan the components of XRD system are a monochromator, a slit set, a detector and a sample holder. The sample is fixed on a holder by clay and its moves by 2θ angle. The detector counts the intensity through an angle of 2θ and the slits are used in order to adjust the size and shape of the x-ray beam of 5.0°/min.

## 3.3 Spectroscopy Experiment Details

A three samples with carbon contact [ AuWWC, AuWLWC-50- and AuWLWC-100-] were prepared to measure the values of impedance (Z), resistance (R), parallel capacitance ($C_p$), series capacitance ($C_s$), conductance(G), reactance(X), and reflectance (ρ) by using an ac signal from impedance analyzer(10MHz-1.8GHz) spectrometer.

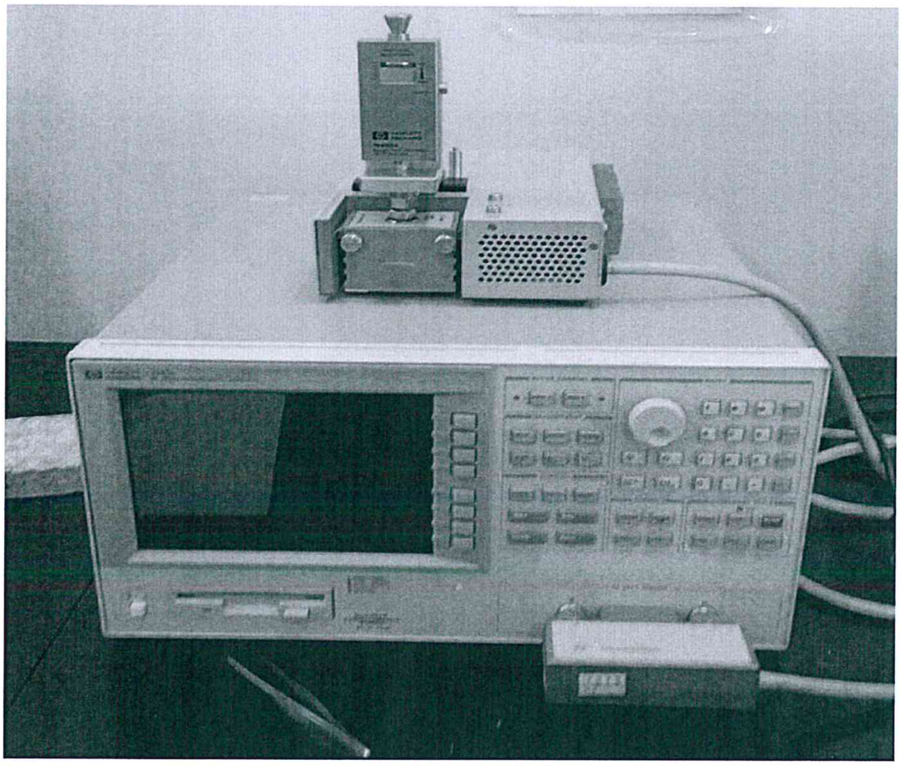

Figure (3.4) Agilent 4291B RF impedance analyzer.

### 3.4 Current-Voltage Measurements

Using Keithley 6485 Pico meter and Keithley 230 voltage power supply connected by MATLAB software packages with a Low-noise coaxial cables to reduce external defects which measures a current in less than 1.0 pA for three samples : AuWWC, AuWLWC-

50- , AuWLWC-100-. The current voltage (I-V) setup at room temperature is shown in figure (3.5).

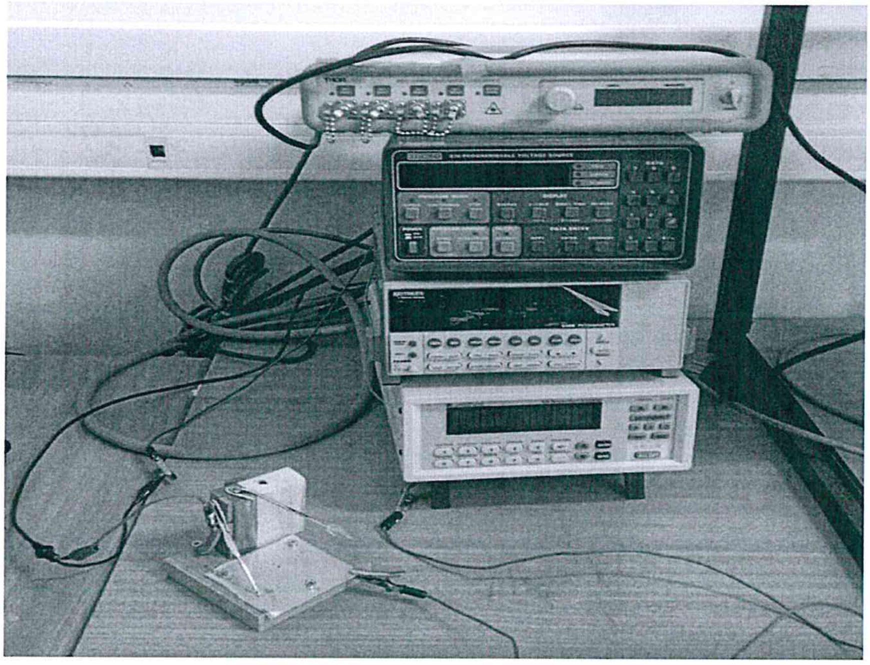

Figure (3.5) The current (I)-voltage (V) characteristic analysis.

### 3.5 Hot Probe Technique

Hot Probe technique is used to determine the type of conductivity the material weather it is n-type or p-type. This test is carried out by using a voltmeter and heater source. The hot probe (which is connected to heater source) is connected with positive terminal of the multimeter while the cold probe is connected to the negative terminal of the multimeter. A positive voltage reading on the multimeter indicating n-type conductivity material while negative voltage reading indicating p-type material. Carroing out this test on the used samples resulting in Lithium (Li) is a p-type and $WO_3$ is a p-type too.

# Chapter Four

# Result and Discussion

## 4.1 Structural X-ray Diffraction (XRD) Characterization

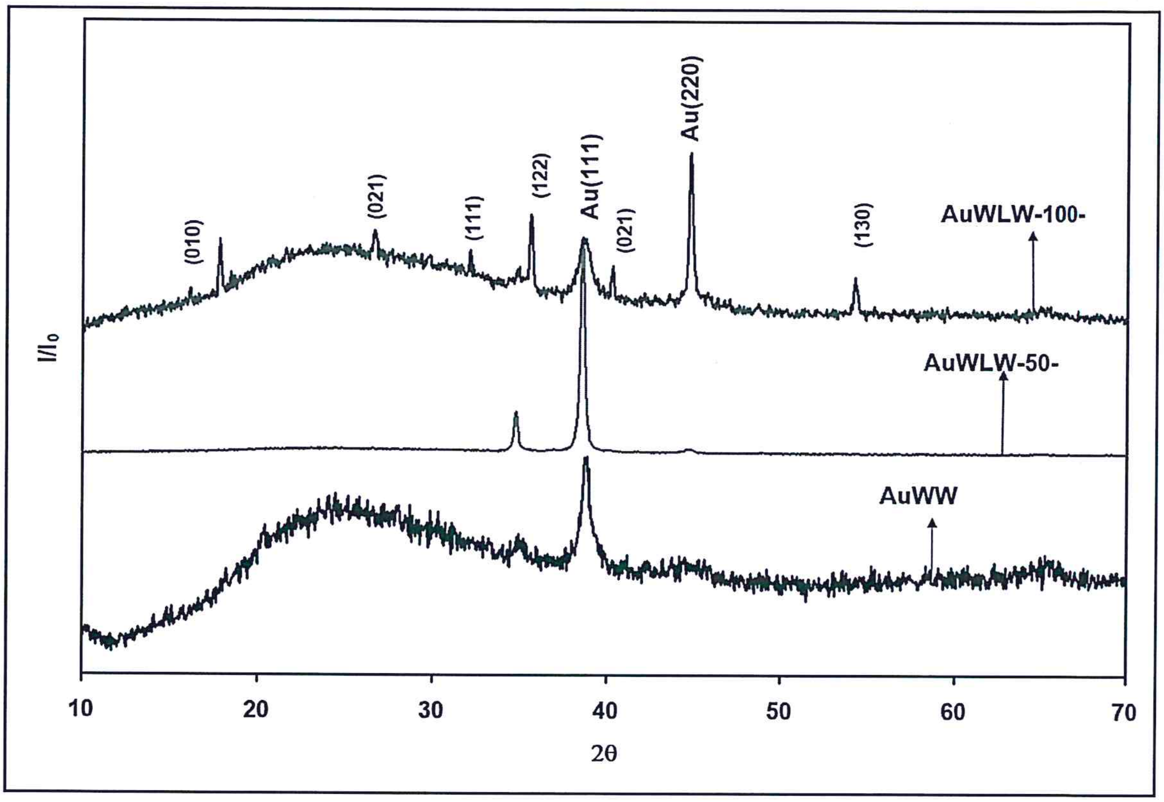

Figure (4.1) : XRD patterns of $WO_3$: Li thin films for different Li thickness

In this study, we will refer the abbreviations AuWLWAu to represent two stacked layers of $WO_3$ comprising Li nano-sheets between its layers (WLW). The three stacked layers are sandwiched between two Au films AuWLWAu. It is evident from the figure that stacked layers of $WO_3$ comprising no Li nano sheets exhibit amorphous structure. The sharp pattern related to face centered cubic gold being best oriented along (111) direction. It is also noted that increasing the thickness of Li layer to 100 nm enhanced the crystallinity of $WO_3$. For AuWLW-100- a strong peaks with mixed phases having a maxima at $2\theta = \{16.3^{\circ}, 26.6^{\circ}, 35.55^{\circ}\}$ with corresponding inter planner distances{0.548,0.334,0.252 Å} due harder in finding the lattice constants the work uses the literature values of $a=7.30$ Å, $b=7.52$ Å, $c=3.84$ Å, $\gamma = \alpha = 90^{\circ}$ and $\beta = 90.76^{\circ}$ [19]. These peaks establish of a monoclinic structure with unknown original at $2\theta = 17.82^{\circ}$, respectively forming the other peaks at $2\theta = \{32.1^{\circ}, 40.3^{\circ}, 54.02^{\circ}\}$ with interring planner distance { 0.279,0.224,0.169 Å} of tetragonal structure type with a calculated lattice constants $a=b=5.3$ Å, $c=4.17$ Å, $\gamma = \beta = \alpha = 90^{\circ}$ [19]. Using Measure software packages, we found 75.49% of the structure is monoclinic and 24.5% is a tetragonal as in addition of the Pd promoter, ZrO2 maintained the same structure as its unprompted analog. In the 12 cases of W-Zr, upon Pd addition weak diffraction lines corresponding to the monoclinic phase appeared, while the diffraction peak corresponding to the tetragonal phase became less intense. Evidently, addition of the Pd complex and calcination led to partial collapse of the original tetragonal phase into the monoclinic phase [20].

Using the Scherrer equation for Nano scale crystallites to calculated the crystallite size (D-nm-), strain ($\varepsilon$), dislocation density ($\delta$-line/cm$^2$) and stacking faults (SF%) from the broadening width ($\beta$-rad-) of all observed peaks using the relations, $D = 0.9\lambda / (\beta \cos(\theta))$, $\varepsilon = \beta/(4\tan(\theta))$, $\delta = 15 * \varepsilon / (D * a)$ and $SF = \pi^2 \beta / (45 * \sqrt{(3 * \tan(\theta))})$, respectively. The calculated structural parameters presented by grain size of D=83.40(nm), and strain $\varepsilon = 1.36 \times 10^{-3}$, and dislocation density of $\delta a = 1.048 * 10^{15}$(line/cm$^2$) are obtained from the broadening of the maximum peak. These parameters including the stacking fault percentages are given in table 4.1.

Table (4.1): Scherrer equation for Nano scale crystallites of the sample $WO_3LiWO_3$-100nm-

| Material | 2θ peak | Ipeak (a.u) | B-rad- $*10^{-3}$ | D-nm- | Strain $*10^{-3}$ | SF% | δ a-monoclinic- |
|---|---|---|---|---|---|---|---|
| $WO_3LiWO_3$-100nm- | 35.6° | 1248.0 | 1.8 | 83 | 1.36 | 0.08 | |

The induced crystallisation by insertion of Li is probably assigned to the insertion process of Li cation between the tungsten oxide(III) with radius of 68-pm- [21] exerted a stress in the bond between W-O with a length of {2.51,1.01 Å } for monoclinic and tetragonal, respectively. That is caused a weaken in the W-O bond leading to form a desirable change to a mixed crystal phase which preferred in fabricating electronic devices. The previous studies explains defects presence in which losing the Oxygen or absorption it indicates to form a sensitive surrounding may lead to a sensor. In recent computational study from a DFT perspective, the nature of O vacancies can be divided according to the basis of different exhibited features:

(1) The density distribution of the excess charge in the ground state and the induced structural relaxation around the defect. In the work of Bondarenko et al investigated polar on hopping in O deficient and lithium doped in monoclinic γ-$WO_3$ using the DFT method calculations on alkali atom intercalated $WO_3$ have also revealed a robust and profound correlation between the electronic properties and the crystalline structure of this material.

(2) The magnetic or nonmagnetic nature of the ground state;

(3) The energy required to create an O vacancy in the pristine material (formation energy).

(4) The electronic properties of the defect states formed in the band gap [22].

The lattice mismatches (Δ%) between Au and $WO_3$, along c-axis are calculated using equation:

$$\Delta\% = \frac{aAu - aWO3}{aAu}$$

Where aAu is the theoretical lattice constant of Au which is equal to 407.8pm and $aWO_3$ the lattice constant of calculated up which in both monoclinic and tetragonal along c-axis. The lattice mismatch between Au and monoclinic of $WO_3$ is 5.8% while the lattice mismatches between Au and tetragonal one is 2.3%. This is large enough to force strained nature of growth of $WO_3$ ,also it explains the extension in the lattice constant . The large lattice mismatch indicates a large quantum confinement, which is showing a fabricated device.

Throughout the XRD analysis, it is noticeable transitions illustrated by the splitting of the maximum peak in figure (4.1) to many reasons like the changes in temperature, pressure, chemical synthesis, which involve internal atomic rearrangements [23].

## 4.2 Impedance Spectroscopy

The impedance spectra for the samples under study are investigated in the spectral range of 10-1800 MHz. The amplitude of the signal is 0.1V. The top contact of the sample was made of carbon. Carbon was selected because it forms good bonding with film surface.

### 4.2.1 Capacitance Spectroscopy:

As illustrated in figure (4.2) the capacitance spectra of AuWWC shows maximum near 0.2 GHz, then it reaches a resonance at 0.423 GHz and anti-resonance at 0.452 GHz after that it remains constant up to 1.4 GHz falls to minimum value. When Li+ nano sheets are participated as shown in figure (4.2-b) multi resonance at 0.091,0.652,0.928 GHz occur and anti-resonance happens at near 0.082,0.616,0.937 GHz, respectively, the resonance–anti resonance peaks it appears the coincidence between the materials Plasmon frequency and the incident AC signal frequency. As the signal frequency exceeds that of Plasmon (limiting) frequency, the electric dipoles loses their ability to feel the incident field and return to its steady state case [24] it shows that negative capacitance effect (NC) which appears due to the negative drain-induced-barrier-lowering instep slope Hysteresis-free Negative capacitance MoS2 Transistors [25]. The correct interpretation of NC can be based on the analysis of the time-domain transient current in response to a small voltage step or impulse, involving a self-consistent treatment of all relevant

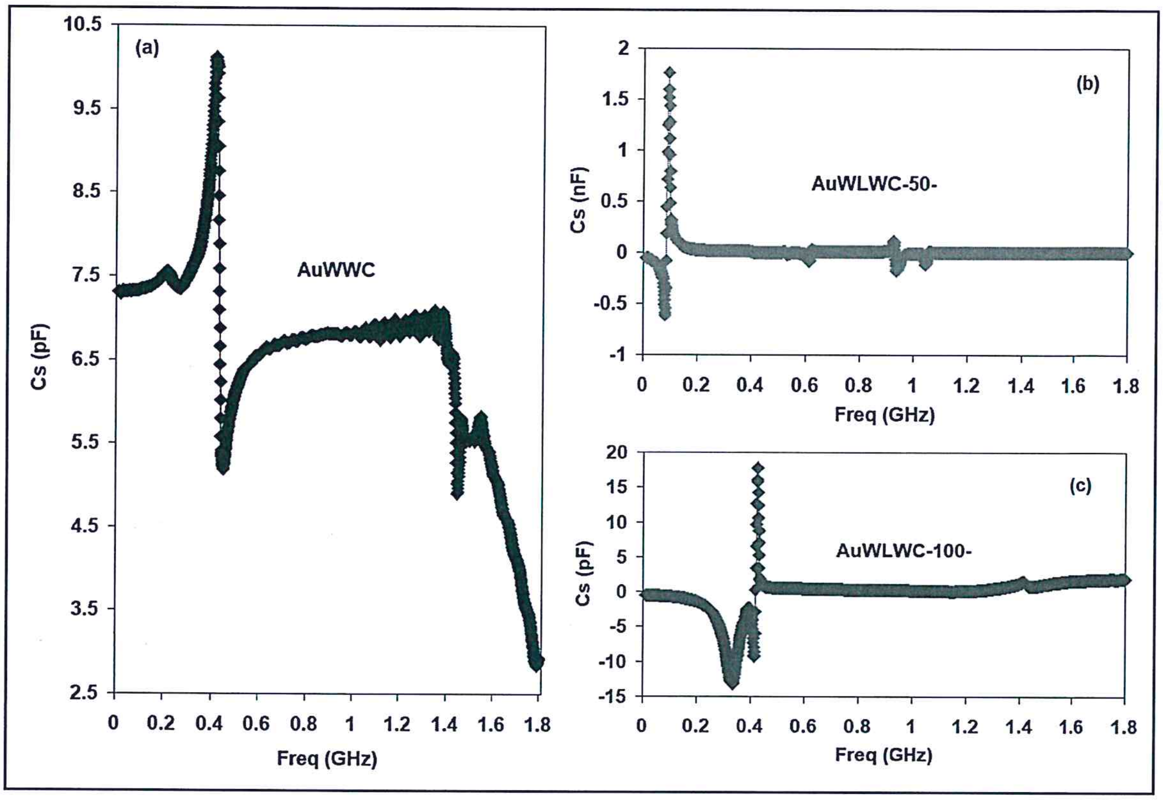

Figure (4.2): The Capacitance spectra of (a) AuWWC, (b) AuWLWC-50-, and (c) AuWLWC-100- samples physical effects (carrier transport, injection, recharging, etc.) [26]. NC appears in the case of the non-monotonic or positive-valued behaviour of the time-derivative of the transient current in response to a small voltage step [15]. NC effects promises to reduce the voltage requirement in conventional complementary metal-oxide-semiconductor transistors below what are otherwise believed to be the Boltzmann limit [14]. The (NC) effects devices are used as noise reducers, parasitic capacitance cancellers and as signal amplifiers. NC effect is reported resulting from the depolarization field that produces a decreasing voltage across the capacitance while the induced charge is increasing. It is also believed that the NC effect could have resulted from a minority charge injection caused by the accumulation of minority carriers at the crystallite boundaries [15]. When increasing Li+ concentration as in figure (4.2-c) also NC appears and a resonance at 0.424 GHz then it remains constant. Capacitance is modelled by Qasrawi-Ershov model to explain the observed resonance and anti- resonance peaks and negative capacitance. Experimental data of the capacitance of three above samples are reproduced in accordance with equation (2.30) and displayed in figure (4.3). The figure indicates good consistence between the experimental and theoretical data. Table (4.2) shows the fitting parameters of capacitance for AuWWC,AuWLWC-50- and AUWLWC-100-.

Table (4.2) Modeled capacitance variables for AuWWC,AuWLWC-50-,AUWLWC-100-.

| Material | $t_n$(s) | $t_p$(s) | $w_n$ (Hz) | $w_p$ (Hz) | $a_1$ | $a_2$ | $C_0$ (F) |
|---|---|---|---|---|---|---|---|
| **AuWWC** | $5*10^{-9}$ | $4*10^{-9}$ | $2.7*10^{9}$ | $2.7*10^{9}$ | 1 | 1 | $7.1*10^{-9}$ |
| **AuWLWC-50-** | $1*10^{-9}$ | $79*10^{-9}$ | $7*10^{8}$ | $5.8*10^{8}$ | 3 | 1 | $1*10^{-12}$ |
| **AuWLWC-100-** | $2.8*10^{-8}$ | $1*10^{-9}$ | $27*10^{9}$ | $21*10^{9}$ | 1 | 13.6 | $1*10^{-12}$ |

From the data illustrated with figure (4.2) there is a decrease in geometrical capacitance $C_0$ from 7.1nF to 1.0 pF as evaporating Li+ ions as the same as the geometrical capacitance decreases in interfacing with the a-$In_2Se_3$ with CdS and decreased more when CdSe is evaporated onto CdS. This is because the three materials exhibit three different statics and high frequency dielectric

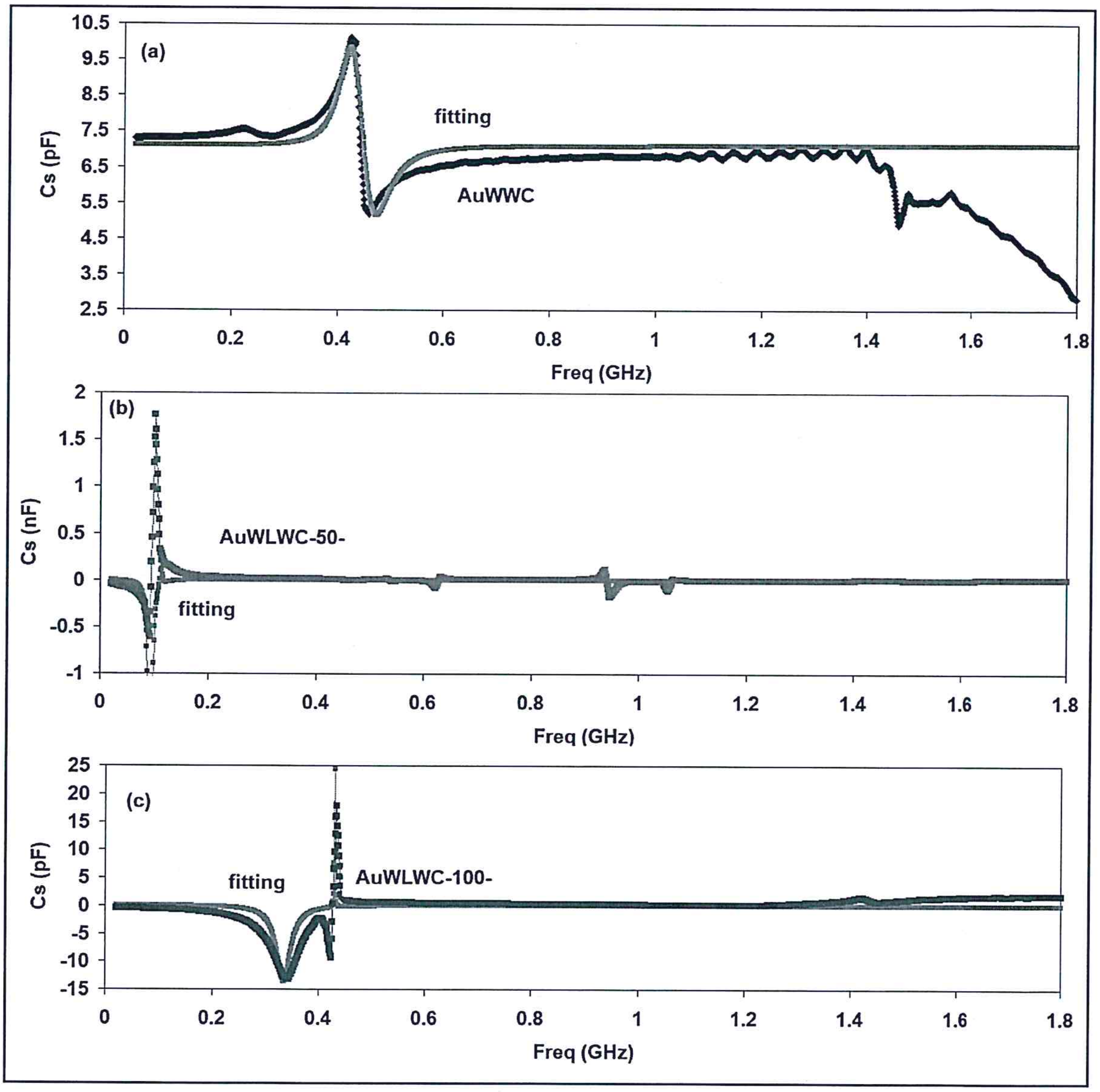

Figure (4.3) The modelled curve of the capacitance of (a) AuWWC, (b) AuWLWC-50-, and (c) AuWLWC-100-

constant values [26]. It is also observed through a direct measurement of negative capacitance in polycrystalline $HfO_2$-based thin films. Other models such as the observation of room temperature sub-60 mV/dec subthreshold slope (SS) in MOSFETs with ferroelectric (FE) layers to propose a model clarifying under which conditions a QS "apparent NC" for an FE layer in a FE-DE bi-layer stack may be observed, quantifying the requirements of strong interface polarization coupling in addition to capacitance matching. In this regime, our model suggests the FE layer does not behave as an NC layer, simply, the coupling leads to both the DE and FE behaving as high-k DE with similar permittivity [27].

### 4.2.2 Conductance Spectroscopy

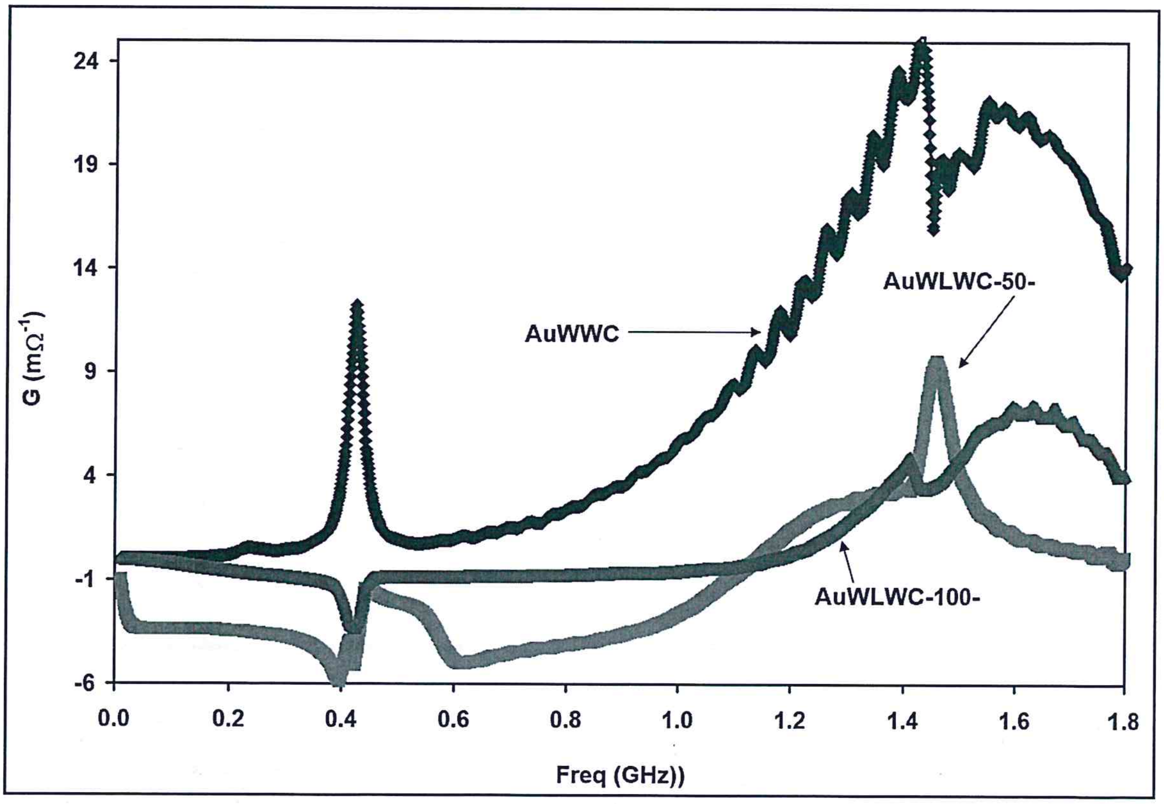

Figure (4.4) Conductance spectra of $WO_3$: Li thin films for different Li thickness
In the range of 0.01-1.8 GHz

AuWWC shows a positive increasing to the curve with a maxima peak at 0.424 GHz then again increase as increasing in frequency and exhibits another two peaks at 1.423. and 1.550 GHz, the AuWLWC-50- G-Freq curve demonstrated a negative G in the interval 0.01-1.1GHz this phenomenon which was observed in In GaAs/InAlAs avalanche photo detector was assigned to the field-induced inter valley transfer excess electrons from the conduction-band minimum to the energetically higher, low-mobility valleys [28]. In addition, AuWLWC-100- has to be curved less rapidly than the two other samples and its maxima around 1.416 GHz.

By doing modeling on conductivity for AuWWC sample and illustrated it in Figure (4.5) using equations(2.34) to calculate the theoretical conductivity we find that

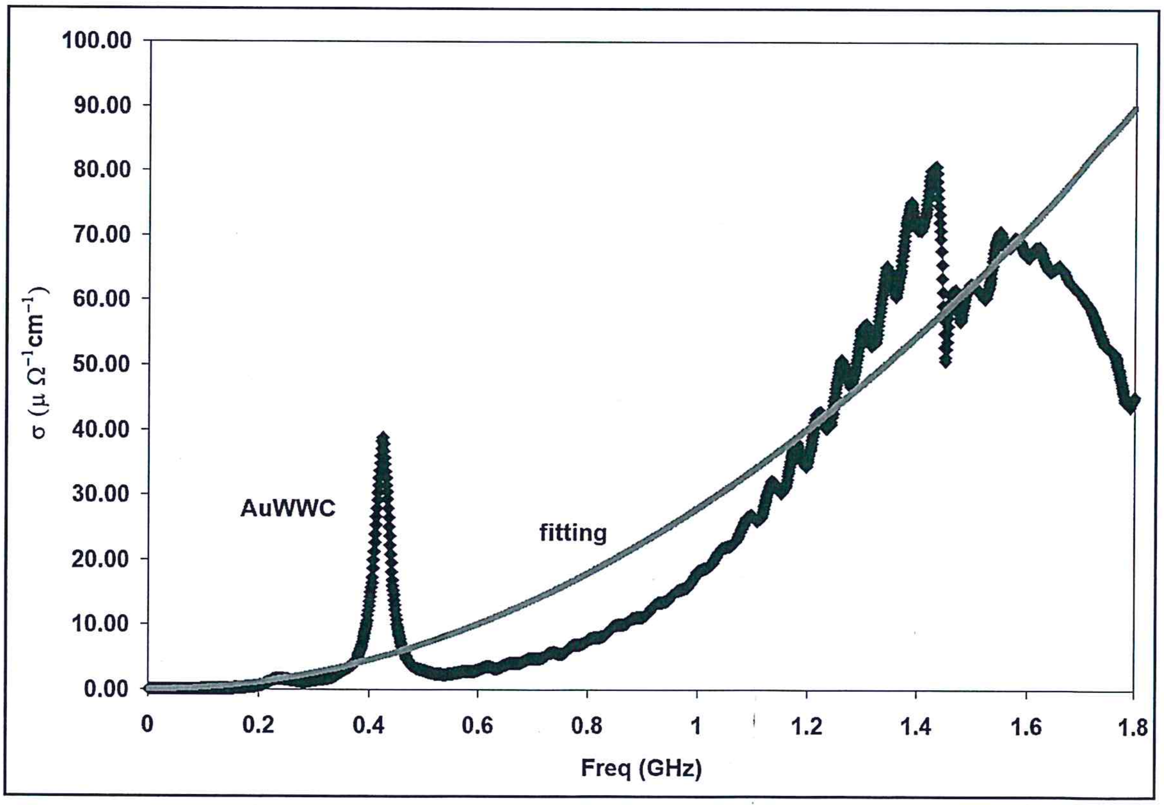

Figure (4.5) Modeled curve of conductivity of AuWWC sample

A well matching between theoretical and experimental approaches according to the calculations with $t_0$ 0.2 ps and $t_{hop}$=0.05 ns these values in table (4.3), there is a complete dominate in the electric conductivity by correlated barrier hoping, having low and high frequency σ(L) and σ(H) conductivities values of $4.0x10^{-9}(\Omega^{-1}cm^{-1})$ and $0.01(\Omega^{-1}cm^{-1})$, respectively. The phonon frequency corresponding a value of ν=166.67($cm^{-1}$), the density of localized states at the Fermi level exhibits a value of N ($E_F$) = 800.0 $x10^{18}$ $cm^{-3}eV$.

Table (4.3) Modeled conductivity variables for AuWWC.

| Variables | Measurement |
|---|---|
| $C_0$ | 45.0(pF) |
| $T_0$(ps) | 0.2 |
| $T_{hop}$(ns) | 0.05 |
| ν $\Omega^{-1}cm^{-1}$) | 166.67 |
| N($E_F$) ($x10^{18}$ $cm^{-3}eV$) | 800.0 |
| σ(L) x ($10^{-2}$ $\Omega^{-1}cm^{-1}$) | 4.0 $x10^{-7}$ |
| σ(H) x ($10^{-2}$ $\Omega^{-1}cm^{-1}$) | 0.01 |

## 4.3 Current-Voltage Characteristics:

Under dark condition and room temperature, the positive terminal of the voltage source is connected to the Au side and the negative electrode is connected to the C side. A direct proportional relationship between Current-Voltage (I-V) is illustrated for the three different thickness of Li as shown in the three figures of figure (4.6). For AuWWC indicates an Ohmic behavior of the compound, as Li+ in figure (4.6-a) for AuWLWC-50- there is no changing in the

Ohmic behavior just the current values become much smaller than in (a) , also in AuWLWC-100- in figure (4.6 b) the attitude of the current does not adapt only become much greater in values, From current-voltage (I–V) measurements of $WO_3$/Ti device, the ohmic-contact implies the formation of the metal-semiconductor junction with very less barrier height ($\varphi_B$) and it helps to the trapping of generated electrons for potential photo detector [29].

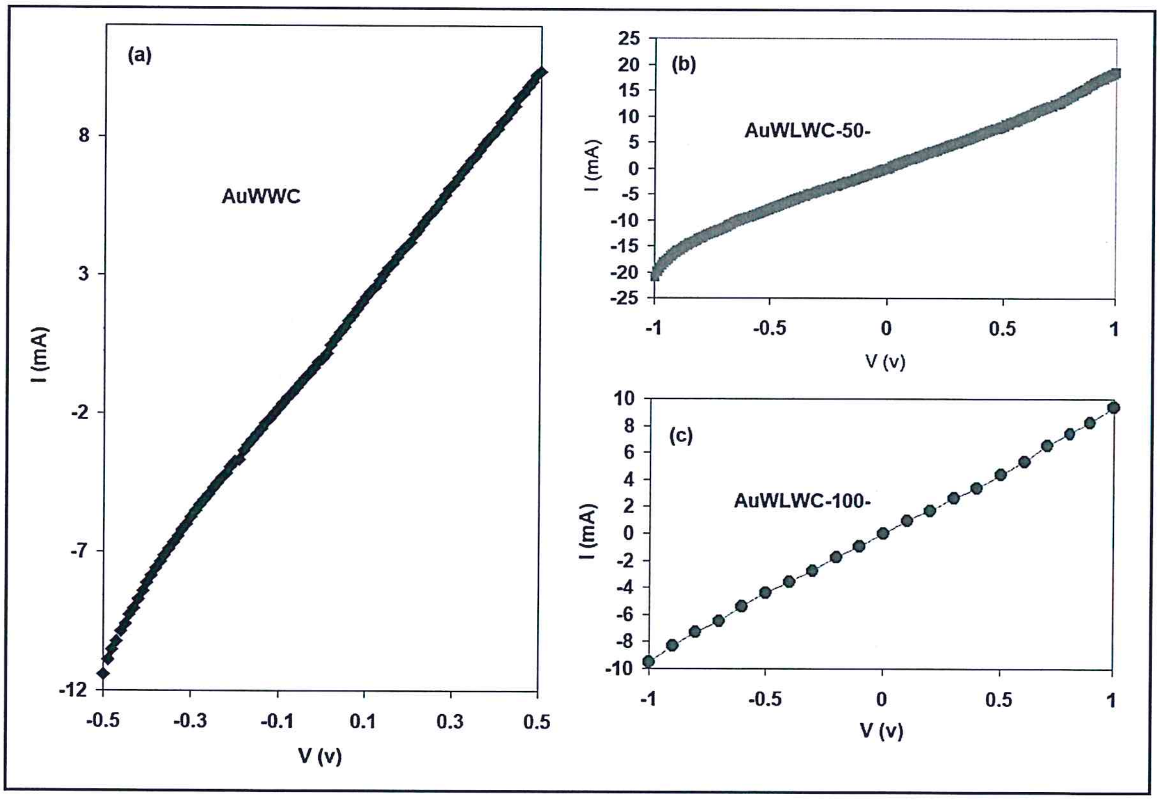

Figure (4.6) The current -voltage characteristics (a) AuWLW-50- (b) AuWLWC-100, and (c) AuWWC

# Chapter Five

## Conclusion

In this thesis, we have studied the structural and electrical heterojunction devices. From the structural analysis, show that the effect of Li layer on the WLW heterojunction obviously through its crystallinity improvement of the films. Furthermore, the increase in Li thickness from 50 to 100 nm leads to decrease in the stress. From the impedance point of view, the AC signal analysis of a AuWWC has small maximum near 0.2(GHz) then it reaches a resonance at (0.423) GHz and anti-resonance at 0.452(GHz), also AuWLW-50nm-multi resonance {0.091, 0.652, 0.928} (GHz) occurs and anti-resonance happens at near {0.082, 0.616, 0.937} (GHz). The resonance–anti resonance peaks is assigned the coincidence between the materials Plasmon frequency and the incident AC signal frequency which indicate the possibility of using the device as a wave trap.Also, Capacitance is modelled by Qasrawi-Ershov model to explain the observed resonance and anti- resonance peaks and negative capacitance .On the other hand, the conductance measurement AuWWC shows a positive increasing in the curve with a maxima peaks at 0.424 GHz then again increase as increasing in frequency and exhibits another two peaks at 1.423. and 1.550 GHz, the AuWLWC-50- G-Freq curve demonstrated a negative G in the interval 0.01-1.1 GHz verified that valley transfer of excess electrons.On the other hand , By doing modeling of conductivity for AuWWC a complete dominate in the electric conductivity by correlated barrier hoping ,having low-and high-frequency $\sigma(L)$,$\sigma(H)$conductivities values of $4.0*10^{-9}(\Omega^{-1}cm^{-1})$,$0.01(\Omega^{-1}cm^{-1})$respectively.

## References:

[1] Zeb, S., Peng, X., Shi, Y., Su, J., Sun, J., Zhang, M., ... & Jiang, X. (2021). Bimetal Au-Pd decorated hierarchical WO3 nanowire bundles for gas sensing application. Sensors and Actuators B: Chemical, 334, 129584..

[2] Dhandayuthapani, T., Sivakumar, R., Zheng, D., Xu, H., Ilangovan, R., Sanjeeviraja, C., & Lin, J. (2021). WO3/TiO2 hierarchical nanostructures for electrochromic applications. Materials Science in Semiconductor Processing, 123, 105515.

[3] Hsini, A., Naciri, Y., Laabd, M., Bouziani, A., Navío, J. A., Puga, F., & Albourine, A. (2021). Development of a novel PANI@ WO3 hybrid composite and its application as a promising adsorbent for Cr (VI) ions removal. Journal of Environmental Chemical Engineering, 105885.

[4] Bonardo, D., Septiani, N. L. W., Amri, F., Estananto, E., Humaidi, S., Suyatman, S., & Yuliarto, B. (2021). Recent Development of WO3 for Toxic Gas Sensors Applications. Journal of the Electrochemical Society.

[5] Peleyeju, M. G., & Viljoen, E. L. (2021). WO3-based catalysts for photocatalytic and photoelectrocatalytic removal of organic pollutants from water–A review. Journal of Water Process Engineering, 40, 101930.

[6] Peleyeju, M. G., & Viljoen, E. L. (2021). WO3-based catalysts for photocatalytic and photoelectrocatalytic removal of organic pollutants from water–A review. Journal of Water Process Engineering, 40, 101930.

[7] Hajirnis, S., Chavan, P., Manapure, V., Patil, A., Khan, A., Nadekar, B., ... & Kadam, A. V. (2021). Hydrothermal synthesis of WO3 film on rough surface to analyze methanol gas at room temperature. *Materials Research Express*, *8*(9), 095503.

[8] Adilakshmi, G., Reddy, A. S., Reddy, P. S., & Reddy, C. S. (2021). Electron beam evaporated nanostructure WO3 films for gas sensor application. Materials Science and Engineering: B, 273, 115421.

[9] Balueva, K. V., Kut'in, A. M. Plekhovich, A. D., Motorin, S. E., & Dorofeev, V. V. (2021). Thermophysical characterization of TeO2-WO3-Bi2O3 glasses for optical applications. Journal of Non-Crystalline Solids, 553, 120465.

[10] Quy, V. H. V., Jo, I. R., Kang, S. H., & Ahn, K. S. (2021). Amorphous-crystalline dual phase WO3 synthesized by pulsed-voltage electrodeposition and its application to electrochromic devices. Journal of Industrial and Engineering Chemistry, 94, 264-271.

[11] Kumar, R., Pathak, D. K., & Chaudhary, A. (2021). Current status of some electrochromic materials and devices: a brief review. Journal of Physics D: Applied Physics.

[12] Lokhande, V., Lokhande, A., Namkoong, G., Kim, J. H., & Ji, T. (2019). Charge storage in WO3 polymorphs and their application as supercapacitor electrode material. Results in Physics, 12, 2012-2020.

[13] Huang, Y., Guo, Z., Liu, H., Zhang, S., Wang, P., Lu, J., & Tong, Y. (2019). Heterojunction architecture of N- doped WO3 nanobundles with Ce2S3 nanodots hybridized on a carbon textile enables a highly efficient flexible photocatalyst. Advanced Functional Materials, 29(45), 1903490.

[14] Zhang, K., Deng, L., Huang, M., Tu, H., Kong, Z., Liang, Z., ... & Wu, Y. (2022). Energy band matching WO3/B-doped g-C3N4 Z-scheme photocatalyst to fix nitrogen effectively. Colloids and Surfaces A: Physicochemical and Engineering Aspects, 633, 127830.

[15] Hajirnis, S., Chavan, P., Manapure, V., Patil, A., Khan, A., Nadekar, B. S., ... & Kadam, A. V. (2021). Hydrothermal synthesis of WO3 film on rough surface to analyze methanol gas at room temperature. Materials Research Express.

[15] Ershov, M., Liu, H. C., Li, L., Buchanan, M., Wasilewski, Z. R., & Jonscher, A. K. (1998). Negative capacitance effect in semiconductor devices. IEEE Transactions on Electron devices, 45(10), 2196-2206.

[16] Qasrawi, A. F., & Hamarsheh, A. A. (2021). Design of Au/Cdbr 2/Au as Negative Capacitance Devices and as Band Filters Suitable for 4G Technologies. Materials Research, 24.

[17] Qasrawi, A., Alharbi, S., & KJhusayfan, N. (2020). THICKNESS AND ANNEALING EFFECTS ON THE STRUCTURAL AND OPTICAL CONDUCTIVITY PARAMETERS OF ZINC PHTHALOCYANINE THIN FILMS.

[18] Ghosh, A. (1990). Frequency-dependent conductivity in bismuth-vanadate glassy semiconductors. Physical review B, 41(3), 1479.

[19] LOKHANDE, Vaibhav, et al. Charge storage in WO3 polymorphs and their application as super capacitor electrode material. Results in Physics, 2019, 12: 2012-2020.

[20] Ji, Y., Bai, S., Xu, D., Qian, D., Wu, Z., Song, Y., ... & Scapens, D. (2020). Pd-promoted WO3-ZrO2 for low temperature NOx storage. Applied Catalysis B: Environmental, 264, 118499.

[21] AL GARNI, S. E.; QASRAWI, A. F. Effect of lithium nano sandwiching on the structural, optical and dielectric performance of MoO3. Physica E: Low-dimensional Systems and Nanostructures, 2019, 114: 113569.

[22] GEROSA, Matteo, et al. Anisotropic effects of oxygen vacancies on velectrochromic properties and conductivity of γ-monoclinic WO3. The Journal of Physical Chemistry C, 2016, 120.21: 11716-11726.

[23]OMAR, A.; QASRAWI, A. F.; GASANLY, N. M. Temperature effects on the structural and optical properties of the TlInSe2xS2 (1− x) mixed crystals (x= 0.3). Journal of Alloys and Compounds, 2017, 724: 98-102.

[24] Si, M., Su, C. J., Jiang, C., Conrad, N. J., Zhou, H., Maize, K. D., ... & Peide, D. Y. (2018). Steep-slope hysteresis-free negative capacitance MoS 2 transistors. Nature nanotechnology, 13(1), 24-28.

[25] Qasrawi, A. F., & Aloushi, H. D. (2019). Formation, negative capacitance and negative conductance effects in Selenium stacked layers sandwiched with Ag nanosheets. Materials Research Express, 6(8), 086435.

[26] Khanfar, H. K., Qasrawi, A. F., & Shehada, S. R. (2019). Negative Capacitance Effect in Ag/α-In 2 Se 3/CdS/CdSe/C Dual Band Stop Filters. Journal of Electronic Materials, 48(1), 244-251.

[27] Kittl, J. A., Obradovic, B., Reddy, D., Rakshit, T., Hatcher, R. M., & Rodder, M. S. (2018). On the validity and applicability of models of negative capacitance and implications for MOS applications. Applied Physics Letters, 113(4), 042904.

[28] Wong, J. C., & Salahuddin, S. (2018). Negative capacitance transistors. Proceedings of the IEEE, 107(1), 49-62.

[29] Yadav, P. K., Reddy, Y. A. K., Ajitha, B., & Reddy, V. R. M. (2020). Oxygen partial pressure dependent UV photodetector performance of WO3 sputtered thin films. Journal of Alloys and Compounds, 816, 15256.

# الملخص

## تصميم وتشخيص رقائق WO3 / Li / WO3 غير المتجانسة

اعداد

شروق سمير مهداوي

اشراف

د. مؤيد أبو صاع و أ.د. حازم خنفر

في هذه الرسالة، استهدفنا استكشاف تأثيرات صفائح الليثيوم النانوية على الخواص التركيبية والكهربائية لأغشية WO3. وتتأثر أغشية WO3 المغطاة بتقنية التبخير الحراري تحت ضغط تفريغ من ١٠-٥ ملي بار بفيلم النانو من الليثيوم. وبالتحديد، أدى إدخال صفائح النانو من الليثيوم بسماكة ٥٠ و ١٠٠ نانومتر إلى عملية التبلور التي يسببها المعدن. تم تقييم مرحلتين هيكليتين نتيجة لتضمين صفائح النانو من الليثيوم. تعود عملية التبلور المستحثة إلى عدم تطابق الشبكة الكبيرة بين الأفلام والركائز والأغشية والألواح النانوية. بالإضافة إلى ذلك، أظهر الفحص الكهربائي الذي تم إجراؤه بواسطة تقنية التحليل الطيفي للمقاومة أنه يمكن أن تعمل الطبقات المكدسة من أكسيد التونغستون التي تشتمل على صفائح النانو من الليثيوم كرنانات ميكروويف. وقد لوحظت ظاهرة الرنين - مضادات الرنين في العينات. علاوة على ذلك، فإن أطياف السعة التي درسناها في مجال التردد من ٠.٠١ إلى ١.٨ جيجاهرتز أظهرت العناصر المهيمنة على تأثير السعة السلبية. هذا التأثير مفيد لإلغاء السعة الطفيلية وتقليل الضوضاء في الدوائر الإلكترونية. علاوة على ذلك، يبدو أن جهاز $WO_3$ / Li / $WO_3$ يُستخدم في التطبيق كغشاء رقيق MOSFET يمكن استخدامه في الدوائر الرقمية والتناظرية.